AIAA JOURNAL
Vol. 41, No. 9, September 2003

Particle Velocity on Solid-Propellant Surface Using X-Ray Real-Time Radiography

Yumin Xiao* and R. S. Amano†
University of Wisconsin–Milwaukee, Milwaukee, Wisconsin 53211
and
Timin Cai,‡ Jiang Li,§ and Guoqiang He‡
Northwestern Polytechnical University, 710072 Xian, People's Republic of China

In a solid rocket motor using aluminized composite solid propellant and submerged nozzle, two-phase flow needs to be investigated by both experiment and computation. The boundary conditions for the ejecting particles constrain their trajectories; hence, these affect the two-phase flow calculations and, thus, significantly affect the evaluation of the slag accumulation. A new method to determine the velocities of particles on the solid-propellant surface was developed, which is based on the x-ray real-time radiography (RTR) technique and coupled with the two-phase flow numerical simulation. A method was developed to simulate the particle ejection from the propellant surface. The moving trajectories of metal particles in a firing combustion chamber were measured by using the RTR high-speed motion analyzer. Image-processing software was also developed for the RTR images so that the trajectories of particles could be obtained. Numerical simulations with different propellant-surface boundary conditions were performed to calculate particle trajectories. By comparing the two trajectories, an appropriate boundary condition on the propellant surface was inferred. The present method can be extended to study the impingement of particles on a wall and other related two-phase flows.

Nomenclature

A	=	area of a pixel-mesh
C_D	=	droplet drag coefficient
d	=	particle diameter
$\boldsymbol{F}$	=	force vector
$f(x, y)$	=	grays on pixel (x, y)
$g(x, y)$	=	grays on pixel (x, y)
I	=	intensity of x rays
L	=	distance
m	=	index
N	=	number of positions
$\boldsymbol{n}$	=	normal vector
$\dot{r}$	=	combustion rate
Re	=	Reynolds number
S	=	neighboring domain
t	=	time
$\boldsymbol{V}$	=	velocity vector
$\boldsymbol{X}$	=	position vector of particles
x	=	x coordinate of pixel
y	=	y coordinate of pixel
α	=	ratio defined in Eq. (11)
β	=	attenuation coefficient
μ	=	viscosity
ρ	=	density
σ	=	standard deviation
ϕ	=	diameter

Subscripts

D	=	drag
g	=	gas
p	=	particle
w	=	weight
0, 1, 2	=	position index

Presented as Paper 2001-1096 at the AIAA 39th Aerospace Sciences Meeting, Reno, NV, 8–11 January 2001; received 1 February 2001; revision received 15 October 2001; accepted for publication 22 October 2001.

*Research Assistant, Mechanical Engineering Department; currently Development Engineer, CFD Research Corporation, Huntsville, AL 35805. Member AIAA.
†Professor, Mechanical Engineering Department. Associate Fellow AIAA.
‡Professor, Department of Power Engineering, College of Astronautics.
§Postdoctorate Fellow, Department of Power Engineering, College of Astronautics.

Introduction

MANY solid rocket motors (SRMs) use aluminized propellants and submerged nozzles to improve performance. When these propellants burn, the aluminum powder melts to form agglomerates on the propellant surface. These agglomerates may move along the surface and then onto the case wall or may be ejected into the gas flow in the combustion chamber, where they burn almost completely to form liquid aluminum oxide (Al_2O_3) droplets. Slag is generated behind the submerged nozzle in two ways; either the agglomerates stream into this region along the case wall or the droplets are trapped in this region (see Fig. 1). The entrapment is affected by the droplet diameter, bulk density, velocity, and position. For boosters of the space shuttle and other larger-scale SRMs the slag accumulation may reach 1000–1500 kg (Ref. 1). Thus, slag simulation is very important for SRM designers to improve the performance of the motor.

The research on slag accumulation has been very active in recent years. Because the cost of experiments is very high and the operation environment is very severe due to high temperature and high pressure, the research in this field is mostly focused on numerical simulation. A simulation technique requires four steps: 1) accurate predictions of the flowfield for the gas phase (selection of a numerical method), 2) knowledge of the distribution of the particle size, 3) modeling of droplet trajectory (particle tracing), and 4) a definition of capture rule, that determines which particles will be retained in the chamber as slag.

Boraas,[2] Haloulakos,[3] Hess et al.,[4] and Meyer[5] conducted extensive modeling of slag accumulation and obtained some useful conclusions. In the 1990s, a number of two-phase compressible viscous computational fluid dynamics codes were advanced for modeling internal two-phase flows in an SRM, for example, Thiokol's SHARP,[6] SRA's CELMINT,[7] and Aerospace's IS.[8] In the mid 1990s, Salita,[9]

Chauvot et al.,[10] and Liaw et al.[11] focused their research on slag behavior, including combustion, evaporation, and breakup. Their work adds insight to the slag accumulation process but, unfortunately, the initial velocities of particles on the solid-propellant surface were chosen arbitrarily in these experiments and the conclusions differed.

Extensive literature exists on the distribution of Al_2O_3 particle size in the combustion products of aluminized composite propellants. Of all the reports, the experimental results of Braithwaite and Salita[12] cover a wide range and seem to provide a reasonable particle-size distribution. Their particle-size distribution function has been widely used by many researchers.

From the preceding discussion it is found that use of a numerical simulation is an efficient tool to study two-phase flow in SRM. The key is to find an experimental method to provide experimental data for some uncertain parameters in the mathematical model to validate the simulation results. Because the operating environment in the combustion chamber is extremely severe (temperature may reach 3500 K and pressure may be over 20×10^6 Pa), it is very difficult to measure the particle velocity in the combustion chamber. The x-ray real-time radiography (RTR) technique is a relatively reliable technology, developed in the 1980s, and provides the possibility of improving this research. Xiao et al.[13] reported some experimental data and proposed a method to determine the ejection velocity of particles on the burning surface. An improved test rocket motor is used in this experiment and better-quality RTR images are presented.

Radiography System

The details of an x-ray RTR system were discussed by Char et al.[14]; thus, only a brief summary is discussed in this section. A schematic diagram of the x-ray RTR system is shown in Fig. 2. A continuous stream of x rays is produced by the x-ray head. The x rays pass through an opening in the first of two lead diaphragms; attenuation occurs as the x rays encounter the test motor and the particles in the combustion chamber. The attenuated x rays pass through an opening in a second lead diaphragm on the other side of the test rig before reaching the image intensifier. The x-ray signal causes fluorescence of cesium iodide on the receiving screen of the image intensifier. The image intensifier transforms the x-ray image into a visible-light image with a time constant of less than 1 μs. This visible image is recorded with a high-speed video camera [up to 6000 frames per second (fps)] and later analyzed with the image-processing system.

Feasibility Analysis

From the aforementioned descriptions of an RTR measurement system, the following features can be deduced:

1) The x-ray intensity distributions on the receiving screen of the image intensifier are affected by the media and its thickness.

2) If the attenuation of x rays by the media can be identified by the x-ray intensifier, this signal may be identified by the naked eye after being augmented.

3) The images recorded by the high-speed recording system are presented as motion pictures.

The flow in the combustion chamber is a gas–solid two-phase flow. Because the attenuation coefficient of the gas to the x rays is much less than that of metal particles, the attenuation of the gas to the x rays is negligible in actual applications. For a single particle, its attenuation to x rays is limited and may not be identified by the x-ray intensifier. Therefore, only those particles whose sizes are large enough to produce attenuation to the x rays and to be identified by the x-ray intensifier can be observed in the experiments. Another fact is that the x rays have to pass through the walls with a relatively high x-rays attenuation coefficient, and the wall thickness of the motor is much larger than the particle size. The intensity variation caused by large particles with a high x-ray attenuation coefficient will be weak and not clear on the image. In the current experimental system, the wall is made of aluminum plate with thickness of 10 mm and the tube voltage is 125 ± 5 kV. I_0, I_1, and I_2 are the x-ray intensities before penetrating the aluminum plate, in the combustion chamber, and after passing through the second aluminum plate, respectively. Table 1 shows the half-value thickness and the x rays attenuation coefficients of several metal materials. Figure 3 shows the layout of x-ray imaging. From Beer's law[14] the following relation can be obtained:

$$I_1 = I_0 \exp(-\beta_1 L_1) \tag{1}$$

$$I_2 = I_1 \exp(-\beta_2 L_3) \tag{2}$$

where $L_1 = L_3 = 0.01$ m, $L_2 = 0.05$ m, and, for aluminum, $\beta_1 = \beta_2 = 0.14$. Because the gray range for a digital image is 256, the smallest size of a particle to be identified on the image should

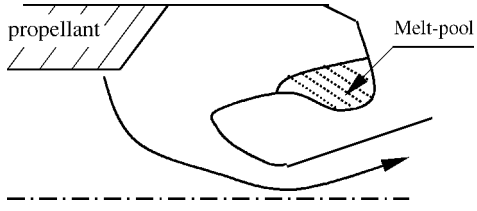

Fig. 1 Layout of an SRM with submerged nozzle.

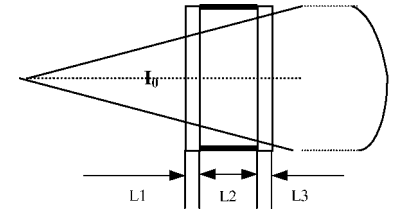

Fig. 3 Layout of x-ray imaging.

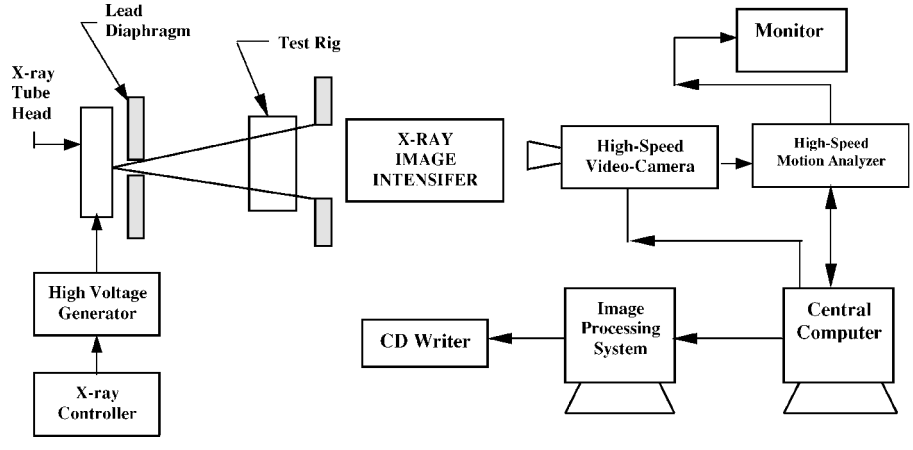

Fig. 2 Layout of the x-ray RTR system.

Table 1 Half-value thickness and x-ray attenuation coefficients

Tube voltage, kV	Half-value thickness, mm			X-ray energy, MeV	Attenuation coefficient				
	Fe	Al	Cu		Fe	Al	Pb	Cu	W
100	2.37	15.1	1.69	1.5	0.37	0.132	0.58	0.41	0.85
150	4.50	18.6	3.50	2.0	0.31	0.150	0.48	0.35	0.71

Table 2 Smallest size to be identified by image processing with tube voltage of 150 kV

Element	Particle size, μm
Fe	130.0
Al	269.1
Cu	113.4
W	56.1
Pb	84.2

satisfy the following relation:

$$|\Delta I| \geq \frac{I_2}{256}\frac{d_p^2}{4A} \tag{3}$$

From Beer's law we have the following:

$$dI = -I_0\beta \exp\left(-\sum_{i=1}^{n}\beta_i L_i\right) dL \tag{4}$$

$$\Delta I = -I_0\beta \exp\left(-\sum_{i=1}^{n}\beta_i L_i\right) \Delta L \tag{5}$$

$$\Delta L_{\min} = -\frac{\Delta I_{\min}}{I_0\beta \exp\left(-\sum_{i=1}^{n}\beta_i L_i\right)} \tag{6}$$

From Eq. (6) and Table 1 the smallest particle sizes that can be identified in image processing for some metal materials are evaluated in Table 2.

The smallest-sized particles listed in Table 2 were deduced from the image identification and from this list we can identify most of the particles in the combustion chamber. However, the identification of particles by the RTR technique is constrained by the resolution of the receiving screen. Because the particles with small size can flow with the gas, the accumulation of slag in the aft domain of the chamber is mainly formed by particles of large size. Our concern focuses on this group. One of the efforts in this paper is an attempt to improve the propellant sample design to ensure that more particles exist on the trace of an x ray.

Experimental Method

From the feasibility analysis described in the preceding section it is concluded that it is possible to measure the trajectory of a particle in a firing SRM combustion chamber. However, in an actual case, the operation is very difficult. The following issues should be resolved before the experiment is set up:

1) The ejection of metal powder. The ejection of particles from a composite propellant burning surface needs to be imitated without scattering the particles in the entire chamber; if the particles are agitated, a moving particle will interact strongly with its neighbors. Therefore, the choice of an aluminized composite propellant as the propellant model is impossible. For this reason double-base propellant was chosen to be the driving force of the metal powder. The powder ejection imitation can be accomplished by putting the metal powder in small holes or narrow slots.

2) The selection of metal particles. A material with a high x-ray attenuation coefficient should be selected. W powder was selected as the metal particle because of its high attenuation coefficient (0.78).

Table 3 Test parameters

Parameter	Value
Combustion chamber	$200 \times 60 \times 50$ (± 0.1 mm)
Propellant sample model	$150 \times 12 \times 50$ (± 0.1 mm)
Slot	0.5 ± 0.01 mm
W powder	$\phi 75 \pm 1$ μm
Operation pressure	$6.75 \pm 0.25 \times 10^6$ Pa
Combustion temperature	2765 ± 10 K

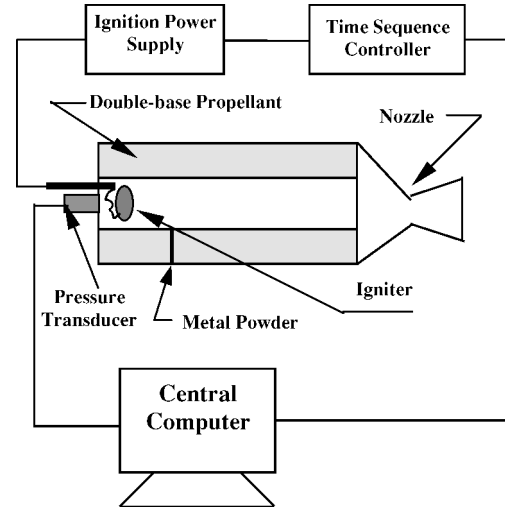

Fig. 4 Layout of test rig.

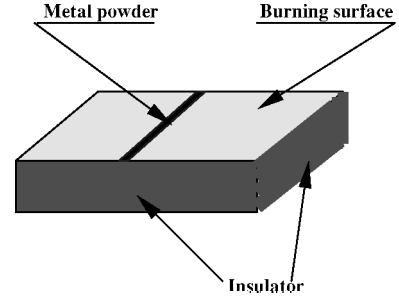

Fig. 5 Layout of propellant model.

Figure 4 shows the layout of the test rig. The central computer sends signals to the time-sequence controller to control the ignition while the pressure signal is recorded by the computer. To enhance the identification of metal particles in RTR images, the following techniques were employed in the experiment:

1) Particles were injected from a narrow slot perpendicular to the flowstream. In this way the projections of particles at the same height would be located at the same pixel on the RTR image and the x-ray attenuation in this position would be several times higher than that for a single particle.

2) The propellant sample and the SRM combustion chamber were made to be two-dimensional.

3) A small focus was used for the x-ray generator to reduce the x-ray intensity from the tube head, which increased its precision.

Figure 5 shows the propellant sample model. The surfaces were insulated, except for the burning surface, to ensure two-dimensionality. Some parameters for the test are shown in Table 3.

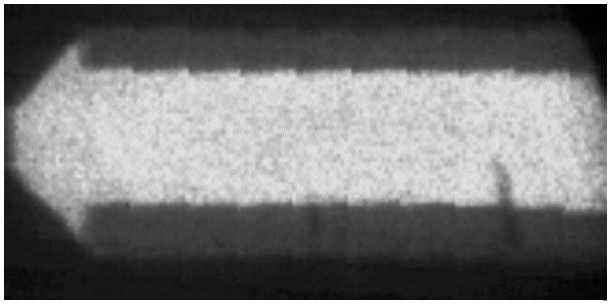

Fig. 6 Typical initial RTR image ($t = 0.408$ s).

Experimental Results

From the basic principle of x-ray image generation it was found that the quality of the image is mainly dominated by the x-ray intensity distribution on the receiver's screen, but it is also affected by the following factors:

1) The experimental system is not in an ideal state. In an actual case, the x rays are not emitted from a single point, which may cause stripes or obscurity on the image. The Compton scattering induced by the walls of the motor and the propellant models will affect the intensity distribution on the screen. Environmental factors such as vibration of the test rig and fluctuation of electric voltage will also affect the image quality.

2) The particle is moving, and the image is projected by a motion picture.

3) The image resolution is constrained by the high-speed motion analyzer. There are 239×192 pixels in one picture and this index is mainly constrained by the processor memory and the high-speed data transportation.

The uncertainty of the system includes two parts: time lag and spatial uncertainty. Time lag is a constant for the whole system and does not affect final data processing, whereas, for the spatial uncertainty, a test was done to determine the magnitude of vibration. With operation pressure $(6 \pm 0.25) \times 10^6$ Pa, the magnitude of vibration in the horizontal plane is less than one pixel. The position dispersion in the RTR image is the main cause of the spatial uncertainty. Usually one position possesses 2–6 pixels in each of the horizontal and vertical directions, respectively. Therefore, the spatial uncertainties of the system are evaluated as ± 1.45 and $\pm 1.56\%$ in horizontal and vertical directions, respectively.

Figure 6 shows a typical initial RTR image. From this image it can be seen that there is a group of particles ejected into the combustion chamber from the burning surface. In any event, the quality of the image shown here is poor and it is difficult to distinguish the particles from the background. Therefore, it is necessary to perform some processing on the initial images to improve the quality. For this reason, image-processing software was developed by the authors[13] to deal with the RTR images; image addition, linear transformation of grays, neighbor-domain averaging, background subtraction, time-domain filtering, and image enhancing were all included. Applications showed that this software is valid for dealing with the trajectories of particles with large diameters (more than 75 μm). Li[15] suggested a method to improve the image quality and resolution. This method is based of the interpolation of the local image information. A Berstein camber is constructed around the pixels of interest and an interpolation can be conducted on a finer grid.

Figure 7 shows the initial sequential images from 0.412 to 0.444 s. It can be seen that the particles were ejected to the combustion chamber almost normal to the burning surface, and after that they moved downstream following the gas.

Droplet Trajectory Modeling in SRM Combustion Chamber

To calculate the trajectory of a particle in the combustion chamber, the gas flowfield may be simulated first. For the present case, the mass fraction of particles in the combustion chamber is very low (particles were ejected from one slot) and the effect of particles on the flow of the gas phase is ignored. There are several methods to simulate the gas flowfield in an SRM combustion chamber, such as via pressure correction methods,[16] the approximate factorization (AF) method,[17] and so forth. In the present calculation the Navier–Stokes equations are solved using the AF method to calculate the flowfield. This code was validated with a test case in a Jet Propulsion Laboratory nozzle by Li,[15] and the calculated results were in good agreement with experimental data.

Usually there are two ways to perform the trajectory calculation: 1) the Lagrangian method, in which particles are considered a dispersed phase and each particle or particle group is followed in a Lagrangian coordinate system, and 2) the Eulerian method, in which both gas and particles are considered continuous phases and can be treated in an integrate method. In the present calculations the Lagrangian method is used to model the particle trajectory, which was applied and validated by Zhou.[18]

The velocity of a particle can be determined by

$$m_p \frac{\mathrm{d}\boldsymbol{V}_p}{\mathrm{d}t} = \boldsymbol{F}_D + \boldsymbol{F}_w \tag{7}$$

and the position of the particle can be determined from

$$\boldsymbol{X}_p = \boldsymbol{X}_p^0 + \int_t^{t+\Delta t} \boldsymbol{V}_p \,\mathrm{d}t \tag{8}$$

The drag force $\boldsymbol{F}_D$ is calculated from

$$\boldsymbol{F}_D = (\pi/8)\rho_g d_p^2 C_D |\boldsymbol{V}_g - \boldsymbol{V}_p|(\boldsymbol{V}_g - \boldsymbol{V}_p) \tag{9}$$

where C_D is determined by

$$C_D = \begin{cases} \dfrac{24}{Re_d}\left(1 + \dfrac{Re_d^{\frac{2}{3}}}{6}\right), & Re_d \le 1000 \\ 0.424, & Re_d > 1000 \end{cases} \tag{10}$$

and where the Reynolds number Re_d is defined as follows:

$$Re_d = \frac{\rho_g |\boldsymbol{V}_g - \boldsymbol{V}_p| d_p}{\mu} \tag{11}$$

Upon integrating Eqs. (7) and (8) the trajectory of the particle can be obtained. However, when integrating Eq. (7) the initial conditions must be assigned: the ejection position and velocity of the particle. When there are no experimental data to provide any information to determine this velocity, one of two assumptions is usually chosen:

1) The particle velocity is set to zero, which indicates that the particles on the burning surface enter the gas under the force induced by the gas drag with zero initial velocity.

2) The particle velocity is set equal to the gas velocity, which implies that there is no delay for velocity equilibrium between the gas and the particle.

As we mentioned earlier, this uncertainty results in a different particle trajectory and thus in a different slag accumulation. Actually, the initial condition is one that lies between the two procedures mentioned earlier. The method used here is summarized as follows:

The initial velocity may be written as

$$\boldsymbol{V}_p^0 = \alpha \left.\boldsymbol{V}_g\right|_{\text{surface}}, \qquad 0 \le \alpha \le 1 \tag{12}$$

where $\boldsymbol{V}_g|_{\text{surface}}$ is the ejection velocity of the gas on the propellant burning surface which can be obtained from

$$\boldsymbol{V}_g = \frac{\dot{r}_p \rho_p}{\rho_g} \boldsymbol{n} \tag{13}$$

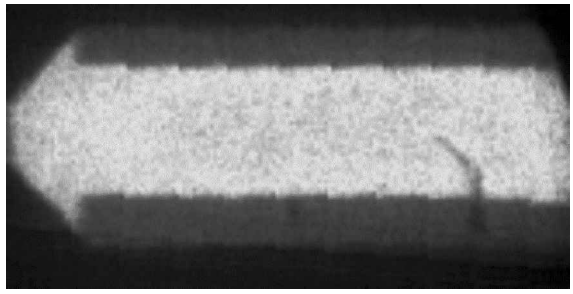

a) $t = 0.412$ s

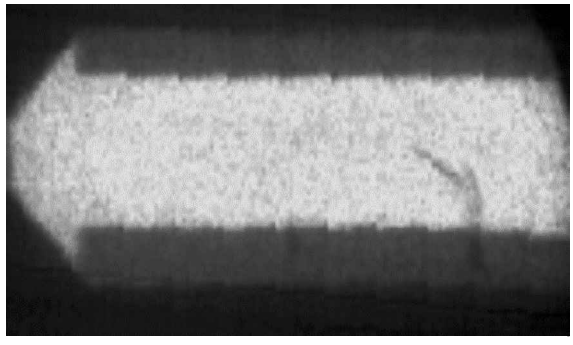

b) $t = 0.416$ s

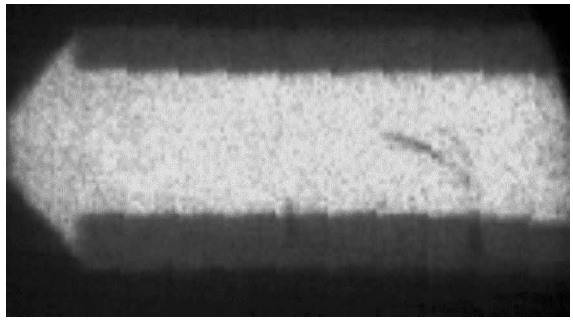

c) $t = 0.420$ s

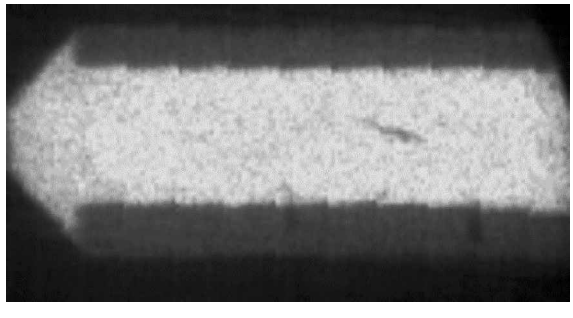

d) $t = 0.424$ s

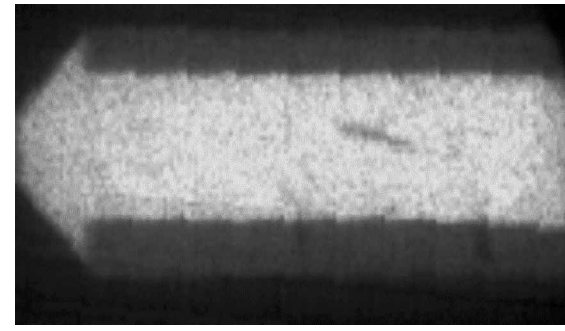

e) $t = 0.428$ s

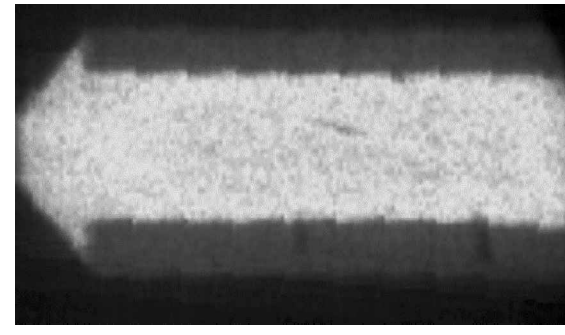

f) $t = 0.432$ s

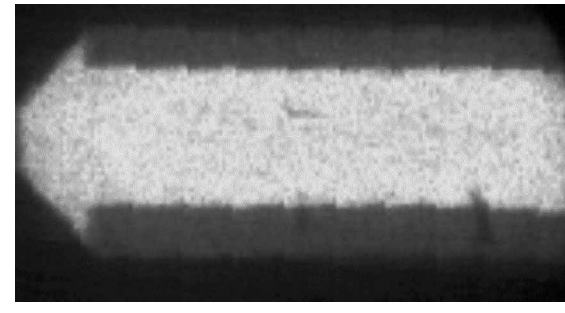

g) $t = 0.436$ s

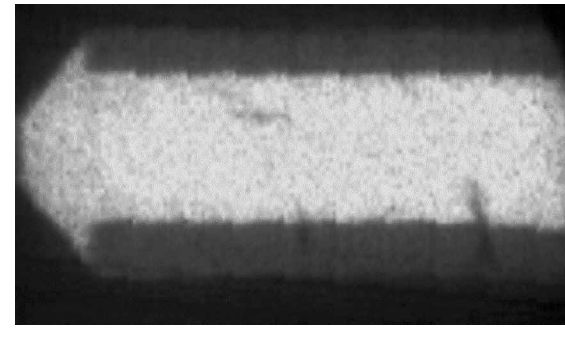

h) $t = 0.440$ s

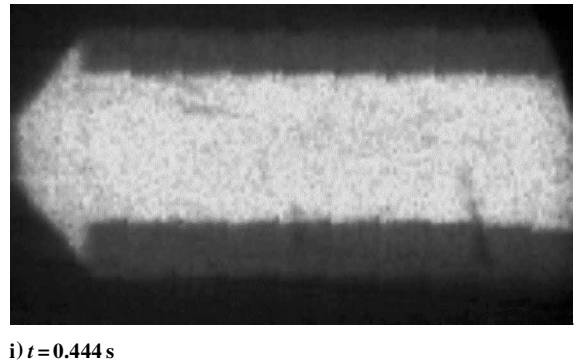

i) $t = 0.444$ s

Fig. 7 Initial sequential RTR images.

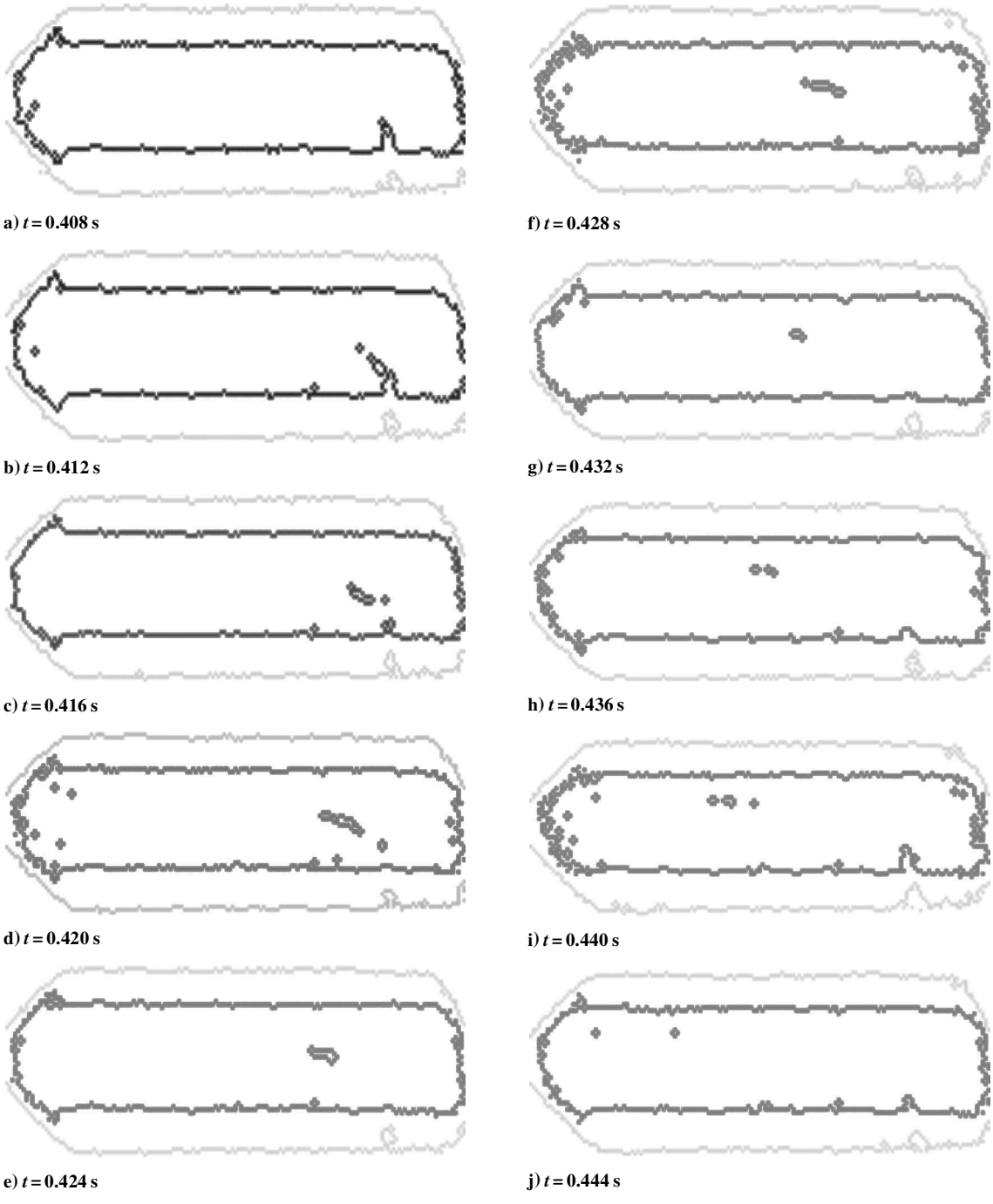

Fig. 8 Sequential RTR images after image processing.

Then a series of values α_i $(0 \le \alpha_i \le 1)$ are chosen and the corresponding $\boldsymbol{V}_p^0$ obtained. From Eqs. (12) and (13), a series of particle trajectories can be calculated. By comparing the calculated trajectory with that obtained from the RTR measurement an adequate value for this case can be deduced. Let (x_i, y_i) be the particle position of the ith node in the RTR image and let (x_i, y_i') be the particle position of the ith node on the calculated trajectory. The standard deviation between two trajectories is defined as follows:

$$\sigma = \sqrt{\frac{\sum_{i=1}^{N} (y_i - y_i')^2}{N}} \tag{14}$$

Here the minimum value from a series of σ can be obtained and then the corresponding α is computed, which will be used to determine the ejection velocity of particles.

Figure 8 shows the sequential RTR images after image processing. Figure 9 shows the particle trajectory obtained by image addition.

As we have noticed, the aforementioned method does not couple the gas-flow solution with the trajectory, which means that the effects of particles on the flowfield are ignored. Therefore, it is valid for flow with a low ratio of solid to gas.

The burning rate of the propellant is 8.3 mm/s. On the burning surface, the gas ejection velocity was imposed, the front end of the combustion chamber was set to be an adiabatic wall, and, at the exit of the nozzle, the flow was supersonic and all parameters were exinterpolated from the inner points.

Figure 10 shows the grid distribution. Figure 11 shows the Mach number distribution in the nozzle. The core flow in the divergent section is approximately one-dimensional.

Figure 12 shows the particle trajectories with different α (0.0–1.0). The particle diameter is 75 μm. It can be found that the particle passes through the symmetrical plane even with zero initial

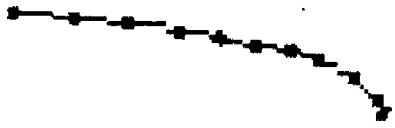

Fig. 9 Particle trajectory obtained by image addition.

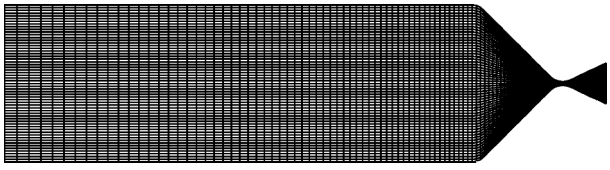

Fig. 10 Grid distributions.

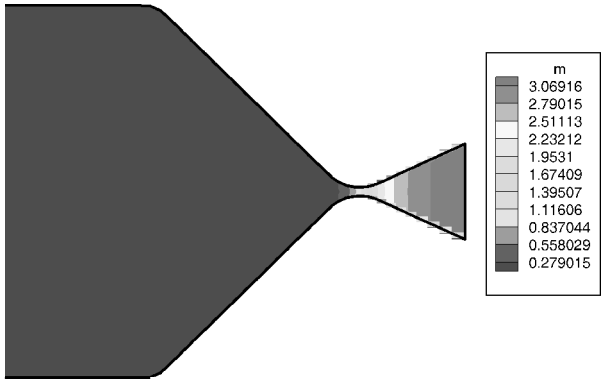

Fig. 11 Mach number contour in the nozzle.

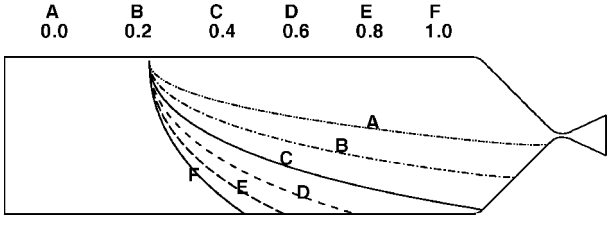

Fig. 12 Particle trajectories with different α ($d = 75$ μm).

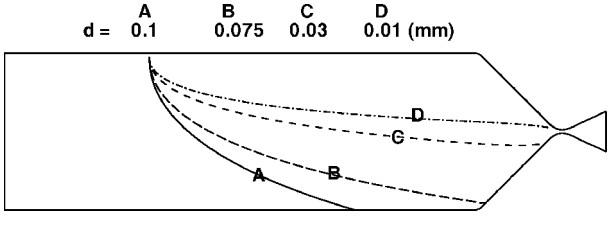

Fig. 13 Particle trajectories with different diameters ($\alpha = 0.4$).

ejection velocity (see trajectory A), which is in agreement with Zhou's conclusion.[18]

Figure 13 shows the particle trajectories with different particle size (diameter ranges from 10 to 100 μm, $\alpha = 0.4$). It can be found that particles with smaller diameter possess good flowability following the gas flow.

To validate the numerical modeling, we compared the calculated trajectory with the measured one. In the present experiments, it was found that when $\alpha = 0.4$ the corresponding σ reaches a minimum. Figure 14 shows the comparison between calculated trajectory and measured trajectory. It was concluded that, with the present initial conditions, the calculated trajectory agrees well with the measured one.

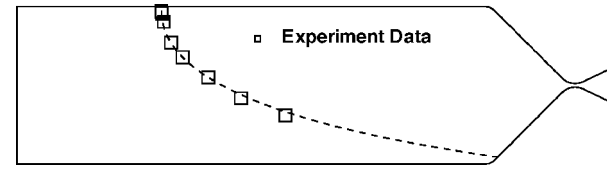

Fig. 14 Comparison between calculation and experiment.

Experiments were performed with particles of small size (25 μm) but the image-processing results were poor. A new kind of image-processing method is being developed by using the subelement interpolation technique to deal with the small particles; the preliminary results show that it was successful for the corresponding cases.

Conclusions

The moving trajectories of metal particles in a firing combustion chamber are measured by using an RTR high-speed motion analyzer. Throughout this study the following conclusions emerge:

1) With the two-dimensional test SRM combustion chamber, the propellant-sample model and particle-ejection model are successfully demonstrated.

2) The metal particles enter into the gas with nonzero initial velocity. The velocity ratio is estimated to be approximately equal to 0.4, which was deduced from a numerical analysis.

3) The proposed method for determining the initial velocity of particles on the burning surface of a solid propellant is demonstrated to be successful. Appropriate boundary conditions for the numerical simulation can easily be obtained.

4) The numerical method and theoretical model are valid for flow with a low ratio of solid to gas.

Acknowledgments

Funding was provided by the National Science Foundation under Grant NSF CTS970045N. The computations were conducted on ORIGIN 2000 at the National Center for Supercomputing Applications, Illinois.

References

[1]Salita, M., "Deficiencies and Requirements in Modeling of Slag Generation in Solid Rocket Motors," *Journal of Propulsion and Power*, Vol. 11, No. 1, 1995, pp. 10–23.

[2]Boraas, S., "Modeling Slag Deposition in the Space Shuttle Solid Rocket Motor," *Journal of Spacecraft and Rockets*, Vol. 21, No. 1, 1984, pp. 47–54.

[3]Haloulakos, V. E., "Slag Mass Accumulation in Spinning Solid Rocket Motors," *Journal of Propulsion and Power*, Vol. 7, No. 1, 1991, pp. 14–21.

[4]Hess, E., Chen, K., Acosta, P., Brent, D., and Fendell, F., "Effect of Aluminized-Grain Design on Slag Accumulation," *Journal of Spacecraft and Rockets*, Vol. 29, No. 5, 1992, pp. 697–703.

[5]Meyer, R. X., "In-Flight Formation of Slag in Spinning Solid Propellant Rocket Motors," *Journal of Propulsion and Power*, Vol. 8, No. 1, 1992, pp. 45–50.

[6]Golafshani, M., and Loh, H.-T., "Computation of Two-Phase Viscous Flow in Solid Rocket Motor Using a Flux-Split Eulerian–Lagrangian Technique," AIAA Paper 89-2785, July 1989.

[7]Sabnis, J. S., De Jong, F. J., and Gibeling, H. J., "Calculation of Particle Trajectories in Solid Rocket Motors with Arbitrary Acceleration," *Journal of Propulsion and Power*, Vol. 8, No. 5, 1992, pp. 961–967.

[8]Chang, I. S., "An Efficient Intelligent Solution for Viscous Flows Inside Solid Rocket Motors," AIAA Paper 91-2429, July 1991.

[9]Salita, M., "Predicted Slag Deposition Histories in Eight Solid Rocket Motors Using the CFD Model EVT," AIAA Paper 95-2728, 1995.

[10]Chauvot, J. F., Dumas, L., and Schmeisser, K., "Modeling of Alumina Slag Formation in Solid Rocket Motors," AIAA Paper 95-2729, 1995.

[11]Liaw, P., Shang, H. M., and Shih, M. H., "Numerical Investigation of Slag Behavior with Combustion/Evaporation/ Breakup/VOF Models for Solid Rocket Motors," AIAA Paper 95-2726, July 1995.

[12]Braithwaite, P. C., Christensen, W. N., and Daugherty, V., "Quench Bomb Investigation of Aluminum Oxide Formation from Solid Rocket Propellants (Part I): Experimental Methodology," *Proceedings of the 25th JANNAF Combustion Meeting*, Vol. 1, CPIA Publications, 1988, pp. 178–184.

[13]Xiao, Y. M., Amano, R. S., Cai, T. M., and Li, J., "Numerical Simulation and Experimental Validation on the Particle Trajectory in a Solid Propellant Rocket Chamber," *Proceedings of ASME 2000 International Design Engineering Technical Conferences and the International 20th Computers and Information in Engineering (CIE) Conference*, American Society of Mechanical Engineers, Paper DETC2000/CIE-14676, 2000.

[14]Char, J. M., Kou, K. K., and Hsich, K. C., "Observation of Breakup Process of Liquid Jets Using Real-Time X-Ray Radiography," AIAA Paper 87-2137, 1987.

[15]Li, J., "A Study on the Motion Pattern of Particles in SRM," Ph.D. Dissertation, Northwestern Polytechnic Univ., Xian, PRC, 1998, pp. 42–48.

[16]Patankar, S. V., "Numerical Heat Transfer and Fluid Flow," *Hemisphere*, Washington, DC, 1980.

[17]Cai, T. M., Xiao, Y. M., and Sun, D., "Numerical Study on Internal Flow Field of SRM with Finocyl Grain and Submerged Nozzle," 49th International Astronautical Congress, IAF-98-S.2.07, 1998.

[18]Zhou, X., "A Numerical Analysis on 2-D Two-Phase Turbulent Flow in Combustor," *Journal of Propulsion and Power*, Vol. 116, No. 5, 1995.

J. P. Gore
Associate Editor